

Modeling phase separation and phase change for magma ocean solidification dynamics

C.-E. Boukaré^{1,2}, Y. Ricard¹ 

¹Université de Lyon, École normale supérieure de Lyon, Laboratoire de Géologie de Lyon, CNRS, 46 Allée d'Italie, 69364

Lyon, France

²Department of Earth, Environmental and Planetary Sciences, Brown University, 324 Brook Street, Providence, RI, 02912,

USA

This article has been accepted for publication and undergone full peer review but has not been through the copyediting, typesetting, pagination and proofreading process which may lead to differences between this version and the Version of Record. Please cite this article as doi: 10.1002/2017GC006902

© 2017 American Geophysical Union

Received: Mar 03, 2017; Revised: Jun 29, 2017; Accepted: Jun 29, 2017

Abstract

Just after accretion, the Earth's mantle was significantly molten by the heat dissipation due to large impacts and to the segregation of the core. The mineralogical observations and thermodynamics models of solid-liquid equilibrium of silicates show that several types of crystallization may have happened at different depths in the mantle. Solids were probably formed first at the bottom of the lower mantle or at mid mantle leaving two possible magma oceans, a shallow one and an abyssal one. Near the bottom of the mantle, the liquid phase might become denser than solids due to iron enrichment. In the shallow magma ocean, the crystallizing solid phase was denser and sank through the magma to settle and compact at depth. To understand these complex dynamics, we develop a two phase numerical code that can handle simultaneously convection in each phase and in the slurry, and the compaction or decompaction of the two phases. Although our code can only run in a parameter range (Rayleigh number, viscosity contrast between phases, Prandtl number) far from what would be realistic, we think it already provides a rich dynamics that illustrates what could have happened. We show situations in which the crystallization front is gravitationally stable and situations where the newly formed solids are gravitationally unstable and can snow across the magma. Our study suggests that the location of a density contrast between solid and magma must be considered of equal importance with that of the intersection between liquidus and isentrope for what concerns mantle solidification.

1 Introduction

Early in the history of terrestrial planets, impact heating [e.g., *Pierazzo et al.*, 1997; *Canup*, 2008], radioactive decay [e.g., *Urey*, 1955; *Castillo-Rogez et al.*, 2009; *Elkins-Tanton*, 2012] and mantle-core segregation [e.g., *Flasar and Birch*, 1973; *Šrámek et al.*, 2012] may have significantly melted the mantle. Subsequent magma ocean evolution depends both on the physical properties of material at relevant $P - T$ conditions and on the complex dynamics of a convecting crystallizing mantle. Fractional crystallization of magma ocean on Earth appears to be a good candidate for explaining the generation of very primitive heterogeneities as those revealed by the studies of the isotopic systems ^{182}Hf - ^{182}W [*Touboul et al.*, 2012]. Present mantle structures such as Ultra Low Velocity Zones (ULVZs) might be directly linked to the crystallization of deep magma oceans [*Labrosse et al.*, 2007]. Basically, scenarios of magma ocean evolution need to answer the

following questions. Where did crystals form? Were these crystals gravitationally stable? What was their subsequent evolution?

The location of incipient crystallization depends on the slope of the melting curve compared to the temperature profile in the magma ocean. Since convection is extremely vigorous in magma oceans, geotherms can be considered as isentropic. According to the accepted values of the Gruneisen parameter (that relates temperature and density along the isentropic profile), Earth's mantle crystallization may have started at the core-mantle boundary [Andrault *et al.*, 2011] or at mid-mantle depth [Fiquet *et al.*, 2010] due to the uncertainties on the Earth's mantle liquidus. Then, the issue of crystal settling or floatation remains first on the sign of the density contrast between solids and liquids. This must be investigated considering two distinct aspects: compressibility and chemical composition.

Several studies have reported that silicate melts exhibit larger compressibilities than solid mantle phases [Stixrude and Karki, 2005; Stixrude *et al.*, 2009]. This observation suggests that melts might become denser than solids at depth in Earth-size planet [e.g., Sanloup *et al.*, 2013]).

Regarding the compositionnal aspect, recent experimental studies have revealed that iron partitions preferentially into the melt [Tateno *et al.*, 2014; Andrault *et al.*, 2012; Nomura *et al.*, 2011]. Consequently, it has been argued that iron enrichment of melt can make liquids denser than solids at high pressure [Thomas *et al.*, 2012; Funamori and Sato, 2010]. More recently, self-consistent investigation of density contrasts between melt and solid during fractionnal crystallization have shown that even if melts are lighter than solids for isochemical compositions (the Clapeyron slopes of end-members such as MgO, FeO, MgSiO₃, related to the liquid-solid density difference, do not change signs), iron-rich melts become easily denser than solids at deep mantle conditions [Boukaré *et al.*, 2015].

Assuming that both melting curves and density contrasts between solids and liquids are known, the most intriguing aspect remains the dynamics of a crystallizing and convecting system. This is the last step to overcome before being able to propose any primordial solid planet's structure.

One of the most challenging aspect remains to describe the intrinsic transient character of a multiphase crystallizing system. At high melt fraction ($\phi \sim 0.95$), highly turbulent convection takes place where melt dynamic dominates crystal segregation. At the

end of the crystallization ($\phi \sim 0.05$), the system mainly exhibits solid-state convection that might be associated with melt percolation if the melting temperature of the residual liquid is low enough. These two end-member dynamic regimes differ significantly because of the viscosity differences between liquid and solid silicates. The almost fully molten system has a very high Rayleigh number ($Ra > 10^{29}$) and inertia dominates whereas solid mantle convection has a lower Rayleigh number ($Ra < 10^{10}$) and can be approximated in the infinite Prandtl number approximation. It must also be noted that low viscosity increases the effects of rotation on planet differentiation [Maas and Hansen, 2015] (i.e., crystal settling in a rotating fluid shell is affected by Coriolis force).

A reasonable strategy is to first study the dynamic of these extreme regimes where the minor phase is diluted. For instance, at high melt fraction ($\phi > 0.99$), the crystals are so diluted that hydrodynamic interactions of particles and their retro-actions on the convecting flow might be neglected. It is thus possible to describe the behavior of the minor phase with a simple parametrization (e.g., particles settling with their Stokes velocities in a convective fluid). When crystal fraction increases, particle interactions become more and more important. A considerable amount of literature (see Faroughi and Huber [2015a] for details) has been published on theoretical approach to investigate both the rheology of fluid systems containing particles in suspension [e.g., Einstein, 1911; Batchelor, 1967] and particle settling velocities [e.g., Batchelor, 1967; Clift et al., 1978]. Several authors have also developed numerical approaches to compute self-consistently settling speed by solving (1) the Newtonian equations for the translation and rotation of each particles and (2) the Navier-Stokes equation for the ambient fluid [Verhoeven and Schmalzl, 2009; Deubelbeiss et al., 2010; Yamato et al., 2012; Suckale et al., 2012]. At high melt fraction, we might assume that crystal settling efficiency depends mainly on crystal size as Stokes speed is proportionnal to the square of the particle diameter [e.g., Solomatov and Stevenson, 1993a; Solomatov, 2007]. Actually, it has been shown that long-range interactions between crystals reduce settling speeds as crystal fraction increases [Suckale et al., 2012; Faroughi and Huber, 2015b] and this phenomena can be observed even in very dilute systems. Hindered settling seems thus as important as crystal size for the issue of segregation in a crystallizing system.

Previous numerical models of crystals segregation in convecting systems were generally based on tracers, representing solid particles (e.g., Suckale et al. [2012]; Verhoeven and Schmalzl [2009]; Höink et al. [2005]). This strategy suffers from two main limitations.

First, the numerical feasibility is limited by the number of tracers. With this approach, numerical modeling of crystal segregation at planetary scale is currently inaccessible. Secondly, the addition, removal or change of sizes of particles during simulation as well as the associated latent heat exchanges in such numerical scheme are tricky. Therefore, the crystal fraction remains unchanged during these simulations. In the case of crystallization of small planetary body such as the Moon, the adiabat falls in between the liquidus and the solidus for the entire mantle. It is thus possible to neglect dissolution of crystals (i.e., removal of tracers) and investigate the issue of crystal settling without phase change. Nevertheless, crystallization/dissolution of crystals might be an important process during the crystallization of larger planets if density contrasts between solid and liquid entrain crystals towards regions with above liquidus temperatures.

The main objective of this study is to develop an understanding of the coupling between convection and phase change for various cases of melting curve profiles and density contrasts between melt and solid. This work thus offers a significant contribution to the studies presented above where settling speed was considered. To understand these complex dynamics, we develop a two phase numerical code that can handle simultaneously the convection in each phase and in the slurry, phase separation (i.e., compaction or decompaction of the two phases) and melting/crystallization. The approach is based on average quantities that allows to deal easily with evolving crystal fraction. The mathematical basis of the code is inspired from the work of *Bercovici et al.* [2001]; *Bercovici and Ricard* [2003] and *Šrámek* [2007]. Other multi phase numerical codes sharing a similar approach have been used by *Schmeling* [2000] and *Wallner and Schmeling* [2016]. The equations are described in the next section.

The key question of this study is to examine the extent to which density contrast between melt and solid governs the evolution of a crystallizing system. Density contrast affects the crystallizing system by driving phase separation. We first test the validity of our phase separation description without phase change. The main particularity of our approach is that we account for phase separation with an equation general enough that it can represent particle settling or Darcy flow. We then couple phase separation mechanism with phase change. We investigate several sets of parameters (sign of density difference between solid and liquid, crystal size...) that are able to produce different kind of crystallization patterns.

Finally, we apply our numerical model to the case of Earth's magma ocean crystallization. We show in a simple scenario that it seems possible to generate a basal magma ocean with a density cross-over between melt and solids even if the adiabat intersects the liquidus at the bottom of the mantle. The formation of a solid layer at mid-mantle depth is somehow similar to the formation of a crust by crystal floatation.

2 A multi-phase model

2.1 Two-phase equations for a silicate mantle: melt and solid

We present the equations for two phases : melt and solid. The two phases, liquid silicate and solid silicate, in volume proportions ϕ and $1 - \phi$ have properties denoted by the subscripts l and s (liquid and solid). We develop our formalism in the Boussinesq approximation where density variations account only for the driving forces in the momentum equation but are neglected in the continuity equation. The densities ρ_s and ρ_l are

$$\begin{aligned}\rho_s &= \rho_0(1 - \alpha T) + \frac{1}{2}\rho_1 \\ \rho_l &= \rho_0(1 - \alpha T) - \frac{1}{2}\rho_1\end{aligned}\tag{1}$$

where ρ_0 is a reference density, the thermal expansivity α is considered equal in the solid and liquid phases, and T is the temperature. The density contrast between liquid and solid, $\Delta\rho = \rho_s - \rho_l$ is equal to ρ_1 which can be constant or depth dependent. The magnitude of the difference between the densities ρ_1 is comparable to the thermal contribution $\rho_0\alpha T$. These density variations are negligible compared to the average density ρ_0 as required by the usual Boussinesq approximation.

The solid-liquid mixture is incompressible and verifies the continuity equation

$$\nabla \cdot \bar{\mathbf{v}} = 0.\tag{2}$$

We use a notation where volume average quantities are denoted with an overscript, e.g., $\bar{\mathbf{v}} = \phi\mathbf{v}_l + (1 - \phi)\mathbf{v}_s$, and difference quantities by a Δ , e.g., $\Delta\mathbf{v} = \mathbf{v}_s - \mathbf{v}_l$ where \mathbf{v}_l and \mathbf{v}_s are the volume averaged liquid and solid velocities. The porosity change is related to the difference in velocities between the two phases (i.e, compaction/decompaction) and the rate of phase change Γ . It satisfies

$$\frac{D\phi}{Dt} = \nabla \cdot [\phi(1 - \phi)\Delta\mathbf{v}] + \frac{\Gamma}{\rho_0}.\tag{3}$$

The Lagrangian derivative includes the advection by the volume average mixture velocity,

$$\frac{D}{Dt} = \frac{\partial}{\partial t} + \bar{\mathbf{v}} \cdot \nabla.\tag{4}$$

Both melt and solid can hold deviatoric stresses even though the viscosity of the melt should be negligible compared to that of the solid. The stress tensor of the solid-liquid mixture is related to the flow by

$$\underline{\tau}_m = \mu_m \left(\nabla \bar{\mathbf{v}} + \nabla^T \bar{\mathbf{v}} \right). \quad (5)$$

where the mixture shear viscosity μ_m depends on the porosity and should be μ_s when $\phi = 0$ and μ_l when $\phi = 1$. The transition between μ_s and μ_l should be rather abrupt [see e. g., *Schmeling et al.*, 2012]. However, in this paper we will only consider a uniform background viscosity $\mu_m = \mu_s$. This is a huge approximation which reduces the parameter space to be explored and decreases the running time of simulations very significantly. At any rate, the viscosity contrast that our code could handle (≈ 2 orders of magnitude) would remain very small compared to realistic solid/magma viscosity contrasts. The total momentum equation for the solid-liquid mixture in the infinite Prandtl number approximation (no inertial forces, we come back later to this approximation) is

$$-\nabla \bar{P} + \nabla \cdot \underline{\tau}_m + \bar{\rho} \mathbf{g} = 0. \quad (6)$$

The melt moves through the matrix according to,

$$c \Delta \mathbf{v} = \phi [\nabla P_l - \rho_l \mathbf{g}], \quad (7)$$

which can be interpreted as a Darcy equation where c is related to the permeability $k(\phi)$ and the fluid viscosity μ_l by $c = \phi^2 \mu_l / k(\phi)$. In this paper, we also made the hypothesis that $k(\phi) = k_0 \phi^2$, this is close to the relations observed experimentally between porosity and permeability and it allows c to be considered as a constant,

$$c = \frac{\mu_l}{k_0}. \quad (8)$$

The solid and liquid pressures P_s and P_l are different (and different from the average pressure of the melt-solid mixture \bar{P}) and a micro-mechanical model (see *Šrámek et al.* [2007]) suggests that they are related by

$$\phi \Delta P = -K \mu_s \nabla \cdot \mathbf{v}_s, \quad (9)$$

where K of order 1 is related to the topology of the melt-matrix interface and we take $K = 1$ in the following. The quantity $K \mu_s / \phi$ takes the same role as the bulk viscosity introduced by *McKenzie* [1984] [see also *Bercovici and Ricard*, 2003; *Wallner and Schmeling*, 2016].

The mechanical equations can be slightly simplified by defining a total non hydrostatic pressure Π ,

$$\nabla\Pi = \nabla\bar{P} - (\rho_0 + \frac{1}{2}\rho_1)\mathbf{g}. \quad (10)$$

Using this definition of Π , the total momentum equilibrium (6) becomes

$$-\nabla\Pi + \nabla \cdot \underline{\tau}_m - \rho_0\alpha T\mathbf{g} - \rho_1\phi\mathbf{g} = 0, \quad (11)$$

showing that the matrix motion is controlled by both the variations of temperature and melt proportion.

Using the mass conservation equation (2), the definition of Π (10), and the expression of the pressure jump (9), the phase separation equation (7) can be recast as

$$c\phi\Delta\mathbf{v} = \phi^2 \left(\nabla \cdot \underline{\tau}_m + \nabla \left[\frac{1-\phi}{\phi} \mu_s \nabla \cdot (\phi\Delta\mathbf{v}) \right] + (1-\phi)\rho_1\mathbf{g} \right) \quad (12)$$

The mechanical equations are supplemented by the energy balance. We assume $\rho_l C_l = \rho_s C_s = \rho_0 C$, and the energy equation writes

$$\rho_0 C \frac{D}{Dt} T = Q + k_T \nabla^2 T + \Gamma L, \quad (13)$$

where Q are the radioactive heat sources, k_T the average coefficient of thermal conductivity and L the latent heat of crystallization. We neglect the various sources of heat related to the flow dissipation.

Finally, we parametrize the rate of change Γ using a simple form of the enthalpy method. Numerically, we apply the phase change after the transport of both temperature and melt fraction. Let T^i and ϕ^i being the temperature and the melt fraction, after transport but before possible melting/crystallization (i.e. solving (3) and (13) with $\Gamma = 0$). T^f and ϕ^f denote these quantities after phase change. Assuming that we can approximate the phase change by a one-component system, liquidus and solidus temperatures, noted T^L are the same. We follow Šrámek *et al.* [2007] in which melting/crystallization is implemented using the following rules,

$$\begin{cases} \text{If } T^i > T^L, \phi^f = \phi^i + \min \left[1 - \phi^i, \frac{C(T^i - T^L)}{L} \right] \\ \text{If } T^i < T^L, \phi^f = \phi^i - \min \left[\phi^i, \frac{C(T^L - T^i)}{L} \right] \end{cases} \quad (14)$$

Then, the temperature is updated using,

$$T^f = T^i - (\phi^f - \phi^i) \frac{L}{C}. \quad (15)$$

This approach is a simplified version of that used by Wallner and Schmeling [2016] for a solid mantle made of two different mineralogic phases.

2.2 Non dimensionalization

We non-dimensionalize lengths by the thickness H of the mantle, time by the thermal diffusion time $\rho_0 C H^2 / k_T = H^2 / \kappa$ (κ being the average coefficient of thermal diffusivity), velocities by κ / H , temperatures by the temperature jump over the mantle ΔT_m and pressure by $\mu_s \kappa / H^2$. Dimensionless quantities are denoted with the superscript $*$, e.g., T^* . Using this scaling, we get

$$\nabla \cdot \bar{\mathbf{v}}^* = 0 \quad (16)$$

$$\frac{D\phi}{Dt^*} = \nabla \cdot [\phi(1 - \phi)\Delta \mathbf{v}^*] + \Gamma^* \quad (17)$$

$$-\nabla \Pi^* + \nabla \cdot \underline{\boldsymbol{\tau}}_m^* + Ra T^* \hat{\mathbf{z}} + Ra B \phi \hat{\mathbf{z}} = 0 \quad (18)$$

$$\phi \Delta \mathbf{v}^* = \epsilon^2 \zeta \phi^2 \left(\nabla \cdot \underline{\boldsymbol{\tau}}_m^* + \nabla \left[\frac{1 - \phi}{\phi} \nabla \cdot (\phi \Delta \mathbf{v}^*) \right] + (1 - \phi) Ra B \hat{\mathbf{z}} \right) \quad (19)$$

$$\frac{DT^*}{Dt^*} = \Delta T^* + Q^* + \Gamma^* S_t, \quad (20)$$

where $\Gamma^* = \Gamma H^2 / \rho_0 \kappa$ and the Rayleigh and buoyancy numbers are

$$Ra = \frac{\rho_0 \alpha \Delta T_m g H^3}{\kappa \mu_s}, \quad (21)$$

$$B = \frac{\rho_1}{\rho_0 \alpha \Delta T_m}.$$

The Stefan number S_t , the normalized permeability ϵ^2 , the viscosity contrast, ζ , and the normalized stress tensor of the solid-liquid mixture, are defined by,

$$S_t = \frac{L}{C \Delta T_m}, \quad (22)$$

$$\epsilon^2 = \frac{k_0}{H^2}, \quad (23)$$

$$\zeta = \frac{\mu_s}{\mu_l}, \quad (24)$$

$$\underline{\boldsymbol{\tau}}_m^* = \frac{\mu_m}{\mu_s} \left(\nabla \bar{\mathbf{v}}^* + \nabla^T \bar{\mathbf{v}}^* \right). \quad (25)$$

Notice that k_0 has the dimension of a surface and represents an effective pore and/or grain cross section in the mixture so that ϵ can be interpreted as the normalized dimension characteristic of the pores and/or grains in the mixture's fabric. We will therefore refer to ϵ as the mixture characteristic dimension. The phase transformation rules (14) and (15) remain formally similar with non dimensional temperatures and L/C replaced by S_t . All the physical quantities used in this paper, with and without dimensions, are listed in Tables 1 and 2.

By using (18), we neglect inertia. In a convective flow, this approximation holds until the Grashof number $Gr = Ra/Pr = \alpha g \Delta T_m H^3 k_T^2 / \mu_m^2$ is of order 1 (or even of order a thousand which is really when turbulence appears [see e.g., *Ricard, 2007*]). This implies that we cannot consider fluid viscosities μ_l smaller than $\approx 10^9$ Pa s. We acknowledge that our model can only explore a parameter space still far away from realistic conditions.

Across a convective two phase domain, we can easily see from equations (20) and (17) integrated across horizontal planes that the total heat flow transported across the fluid is,

$$Q = \langle \bar{v}_z^* T^* \rangle - \frac{d \langle T^* \rangle}{dz^*} + S_l \langle \bar{v}_{lz}^* \phi \rangle, \quad (26)$$

where the brackets are horizontal averages. The three terms of the right side express the transport of heat by convection, diffusion and latent heat, respectively.

2.3 Numerical implementation

The numerical code is a variant of the code used and discussed in *Šrámek [2007]* and *Šrámek et al. [2010]*. The mechanical equilibrium equations for total momentum (2) and (18) are identical to those for a single incompressible phase. We solve these equations on a staggered grid with a direct implicit inversion method after expressing the solenoidal vector field $\bar{\mathbf{v}}^*$ using a stream function [*Schubert et al., 2001*]. We use free slip boundary conditions on the four sides.

To solve equation (19) we first introduce $D = \nabla \cdot (\phi \Delta \mathbf{v}^*)$ which satisfies an equation obtained by taking the divergence of (19),

$$D - \epsilon^2 \zeta \nabla \cdot \left[\phi^2 \nabla \left(\frac{1 - \phi}{\phi} D \right) \right] = \epsilon^2 \zeta \nabla \cdot (\phi^2 \mathbf{F}) \quad (27)$$

where,

$$\mathbf{F} = (\nabla \cdot \tau_m^* + (1 - \phi) Ra B \hat{\mathbf{z}}) \quad (28)$$

The boundary conditions for D are found when equation (27) is integrated across the boundary of the computing box, perpendicular to the normal \mathbf{n} . One obtains that, on the boundaries of the convecting domain,

$$\mathbf{n} \cdot \nabla \left(\frac{1 - \phi}{\phi} D \right) = \mathbf{n} \cdot \mathbf{F} \quad (29)$$

Equation (27) with boundary conditions (29) are again solved with a direct implicit inversion method as the forcing term (28) is known after the resolution of the total momentum

	Symbol	Value	Unit
Melt viscosity	μ_l	$10^{-1} - 10^3$	Pa s
Solid viscosity	μ_s	$10^{18} - 10^{21}$	Pa s
Mantle density	ρ_0	4×10^3	kg m^{-3}
Mantle depth	H	3×10^6	m
Thermal expansion	α	2×10^{-5}	K^{-1}
Thermal diffusivity	κ	10^{-6}	$\text{m}^2 \text{s}^{-1}$
Thermal capacity	C	10^3	$\text{J kg}^{-1} \text{K}^{-1}$
Latent heat of melting	L	10^6	J kg^{-1}
Solid-liquid density contrast	ρ_1	$-250/+500$	kg m^{-3}
Gravity	g	10	m s^{-2}
Temperature difference	ΔT_m	3×10^3	K
Solidus/Liquidus slope approximation ^a	$\partial_z T_{s/l}$	0.83	K km^{-1}
Magma Ocean's adiabat approximation ^b	$\partial_z T$	0.6	K km^{-1}
Permeability constant ^c	k_0	-	m^2

Table 1. Physical parameters. ^a[Andrault *et al.*, 2012]. ^b[Thomas *et al.*, 2012]. ^c we assume $k(\phi) = k_0\phi^2$.

Both the slope of the liquidus and the slope of the adiabat are a matter of debate [Fiquet *et al.*, 2010; Moserfeldt *et al.*, 2009; Thomas *et al.*, 2012]. In this study, we focus on the influence of the density contrast on the crystallization for given liquidus/adiabat situation.

equation (18). Once D is obtained, the right hand side of (19) can be directly computed and therefore $\phi\Delta\mathbf{v}^*$ is known, and as \mathbf{v}^* is also known, we deduce \mathbf{v}_s^* and \mathbf{v}_l^* .

Temperature and melt fraction are advected using an alternate directions scheme [Peaceman and Rachford, 1955] supplemented by the flux limiter "superbee" [Roe, 1985; Šrámek *et al.*, 2010]. Temperature is imposed at the bottom ($T^* = 1$) and the top ($T^* = 0$) of the domain.

	Symbol	Magma Ocean	This study
Rayleigh Number	Ra	$10^8 - 10^{30}$	$10^6 - 10^7$
Prandtl number	Pr	$1-10^{22}$	∞
Buoyancy	B	$-1 < B < 2$	$-1 < B < 2$
Stefan number	S_t	0.3	0.3
Viscosity contrast	ζ	$10^{15} - 10^{22}$	1
Mixture characteristic size	ϵ	-	$1 \times 10^{-4} - 1 \times 10^{-1}$

Table 2. Dimensionless physical parameters.

3 Settling velocity and sedimentation efficiency

Modeling dynamics of magma solidification requires to add two key processes to thermochemical convection: phase separation and phase change. In the next subsections, we first test these two aspects separately before applying this numerical model to the case of Earth's magma ocean. Even though our model is definitively not able to be used in a realistic regime for magma ocean, we show that our approach is able to capture crucial aspects of magma solidification dynamics that might then be transferable to more turbulent regime.

3.1 General approach

One of the most important aspect of magma crystallization dynamics is the sedimentation (more broadly phase separation) efficiency. This latter is related to whether a planet experiences fractional crystallization (i.e., the newly formed crystals sink or rise and segregate from the magma) or batch crystallization (i.e., crystals remain entrained and in equilibrium with their "parent" liquid). It thus controls, to some extent, the primordial chemical stratification generated by crystallization.

Sedimentation efficiency can be investigated via several criteria (see *Solomatov* [2007]). A rough estimate can be obtained by comparing a typical convective velocity with a set-

Figure 1. Convective velocity (red) compared to settling velocity (blue). According to our mathematical formalism, the mixture characteristic size ϵ plays here the same role as a particle radius (see (32)). For a magma with viscosity values as low as 0.1 Pa s (see Table 1 for the other parameter values), we expect a Rayleigh number around 10^{30} and typical convective velocities of about a few m s^{-1} . A Stokes formula (31) with such a low viscosity value gives a rough estimate of the critical crystal radius (1-3 cm) above which crystals settle. Increasing the viscosity of the system (to reach the feasibility domain of the numerical simulation), decreases both convective and settling velocity. The issue of crystal settling remains valid, the critical crystal size is just shifted.

ting velocity [*Huppert and Sparks*, 1981]. Nevertheless, this neglects the fact that convective velocities should be regarded as a statistical distribution [*Martin and Nokes*, 1988, 1989]. An alternative approach is to estimate the amount of energy available (taken from thermal convection that overcomes viscous friction) to suspend crystals [*Solomatov and Stevenson*, 1993b]. Since this quantity is difficult to estimate, *Solomatov and Stevenson* [1993b] have proposed to consider a more severe limit at which the amount of energy released per unit time due to crystal settling exceeds the total amount of energy per unit

time available for mechanical work (i.e., the total heat loss rate of the system). All of these considerations end up with a critical crystal size below which crystals are simply entrained because settling is a competition between a body force, the weight, and surface force, the viscous friction. Therefore, the issue of element fractionation has been transferred to the question of crystal sizes and crystal growth which remain very challenging at magma ocean conditions [Solomatov and Stevenson, 1993a; Solomatov, 1995].

In this paper, we assume that the ratio of the relative velocities of crystals ($\Delta \mathbf{v}$) compared to convective velocities ($\bar{\mathbf{v}}$) is sufficient to capture the first order signature of the crystallization process. In a magma ocean in a state of hard turbulence convection with $Ra \approx 10^{30}$ (a viscosity is order 0.1 Pa s), the magma velocities are likely around 1-10 m s⁻¹ [Solomatov, 2007]. Such a velocity corresponds to the Stokes velocity of particles of radius 1-3 cm with a buoyancy number of $B = 2$ (i.e. a solid-liquid density contrast $\Delta\rho$ of 480 kg m⁻³, see Table 1). Particles larger than this critical size should segregate, smaller particles should be entrained. Even if the Stokes velocity seems to be a crude approximation, the reader should bear in mind that more rigorous estimations do not differ significantly and predict a critical size of about 1 mm [Solomatov, 2007]. These extreme conditions of solid liquid convection and segregation are far from being accessible by current numerical simulations. We only investigate solidification dynamics at a very modest Rayleigh number of 10^6 ($\mu_m = 6.5 \times 10^{22}$ Pa s) and an average surface velocity of $v_s \approx 1$ cm yr⁻¹ in which case only blobs of about 139 km radius can segregate ($B = 2$ and $\Delta\rho = 480$ kg m⁻³, see Figure 1). In our code however, the size of the crystal does not appear and only the local liquid fraction ϕ , is monitored. However the mixture characteristic size, ϵ plays the same role as crystal size. Using the equation (12), the definitions of c , (8), and ϵ^2 , (23), and assuming a uniform melt fraction, we can obtain a solution for the phase separation velocity,

$$\Delta \mathbf{v} = \phi(1 - \phi) \frac{\rho_l \mathbf{g} \epsilon^2 H^2}{\mu_l}. \quad (30)$$

Considering that the liquid is at rest ($\mathbf{v}_l = 0$), we can identify equation (30) with a Stokes formula of the form,

$$\mathbf{v}_s = \frac{2}{9} \frac{\rho_l \mathbf{g} R^2}{\mu_l}, \quad (31)$$

where R is the radius of the settling particle. It turns out that we can associate ϵ with a crystal size R by,

$$\epsilon H \sqrt{\phi(1 - \phi)} \approx \frac{1}{2} \epsilon H = \frac{\sqrt{2}}{3} R. \quad (32)$$

This suggests that for the Rayleigh number that we can reach, we should use ϵ of order 10^{-2} to capture the solid-liquid separation, i.e., a mixture characteristic size ϵ of the same order as the normalized radius of tracers, R/H in an equivalent convection code with Stokes tracers (see Figure 1).

3.2 Results

We verify this prediction with the numerical experiments. We run a 2D Rayleigh-Bénard convection experiment at $Ra = 10^6$ and $\zeta = 1$ ($\mu_m = 6.5 \times 10^{22}$ Pa s) until a steady state or stationary steady state regime is obtained. We then assume solid fraction of $\phi = 0.5$ and buoyancy number $B = 2$. We ran five simulations with different mixture characteristic sizes: 0.5×10^{-3} , 10^{-3} , 5×10^{-3} , 0.01 and 0.05. According to the equivalence (32), the solid-liquid separation that our code simulates, corresponds to the segregation of tracers of radiuses of 1.59, 3.18, 15.9, 31.8 and 159 km, that should sink with Stokes velocities of 1.31×10^{-4} , 5.26×10^{-4} , 1.31×10^{-2} , 5.26×10^{-2} and 1.31 cm yr^{-1} and cross the half mantle after normalized times of 4, 1, 0.04, 0.01 and 4×10^{-4} , respectively. The repartition of solids at time t is tracked by computing the average liquid proportion, $\phi_M(t)$, in the upper half of the box (likely varying between 0.5 when the phase content is homogeneous to 1 for complete segregation (see Figure 2)).

Figure 2 depicts the evolution of ϕ_M as function of the dimensionless time. For mixture characteristic sizes lower than 5×10^{-3} , we observe that ϕ_M remains around 0.5. This means that solids cannot settle in these conditions (i.e., small crystals). They are re-entrained by the convective flow. For mixture characteristic sizes values higher than 5×10^{-3} , we clearly see that ϕ_M tends to a value close to 1, and in a time comparable to the time needed by a dense tracer with the radius given by (32) to sediment. This means that solids settle and accumulate at the bottom of the domain. The larger the mixture characteristic size, the faster solids segregate from the magma. We note that even with small mixture characteristic times that correspond to tracers with Stokes velocities smaller than the average convective velocity, some segregation occurs (e.g., for $\epsilon = 5 \times 10^{-3}$).

We plot in Figure 3 the histograms for the distribution of vertical convective velocities (v_z , in red) and vertical phase separation velocities (Δv_z , in blue) for the five sim-

Figure 2. Evolution of the average liquid fraction in the upper half of the box through time ($Ra = 10^6$, $\zeta = 1$, $B = 2$, no phase change). For mixture size values below 5×10^{-3} , solids are entrained by the flow. When the mixture size is larger than around 5×10^{-3} , solids settle. The larger the mixture size (i.e., particle size), the faster the segregation.

ulations. The horizontal axis are the velocities in cm yr^{-1} , the height of the histograms is proportional to the volume of the flow having a given velocity. These histograms are computed for different mixture characteristic lengths (ϵ , left vertical axis). At $t = 0$ (Figure 3a), all convective velocities follow exactly the same distribution. The average convective velocity is close to the value predicted by a scaling law (about 1 cm yr^{-1} , which agrees with the velocity-Rayleigh number scaling law, $\langle u \rangle = 0.2(\kappa/H)Ra^{3/5}$ proposed by [Pandey *et al.*, 2014]. The major part of the system shows convective velocity between 0.1 and 0.9 cm yr^{-1} but there is a non negligible part of the domain that shows convective velocities lower than 0.1 cm yr^{-1} . We discuss later the location of these zones. Figure 3a also clearly shows that the initial phase separation velocity matches closely the solution given by (30) (blue line). As mixture size increases, the number of fluid parcels where

the settling velocity is higher than the convective velocity increases as well. Later in the simulation (Figure 3b), when some phase separation has taken place (the corresponding snapshots are depicted in Figure 4), we observe that the velocity distribution remains the same for $\epsilon \leq 5 \times 10^{-3}$. In these cases, we argue that settling velocity is so low that it does not affect the fluid dynamics and no segregation occurs. Nevertheless, we see that a settling velocity of about $1.31 \times 10^{-2} \text{ cm yr}^{-1}$ (obtained with $\epsilon = 5 \times 10^{-3}$) is enough to produce crystal settling when $Ra = 10^6$. In this case, even though the settling velocity is more than two orders magnitude lower than the maximum convective velocity, crystal settling is possible in some places. This statistical analysis also indicates that the distribution of convective velocities is shifted to lower values when segregation occurs. The latter is consistent with the fact that convection is stopped if sedimentation rate exceeds the available mechanical power [Solomatov and Stevenson, 1993b].

In order to better characterize crystal settling in these simulations, we plot in Figure 4, 2D maps of the difference between $|\Delta v_z|$ and $|\bar{v}_z|$ together with 2D maps of the accumulation rate $\partial_t \phi$. Comparing these quantities allows us to clearly distinguish regions where the separation flow is more active than the average flow (i.e., $|\Delta v_z| > |\bar{v}_z|$) and regions where crystals accumulate (i.e., $\partial_t \phi > 0$). These snapshots have not been taken at the same time (the timescale of the segregation are very different depending on the mixture size, see Figure 2) but they are representative of the structure of the 2D velocity field during segregation. For mixture sizes below 5×10^{-3} , we do not observe any sizable regions where phase separation is stronger than convective velocities as previously pointed out by the statistical analysis presented above. For very large mixture sizes ($\epsilon > 0.05$), settling velocity is stronger than convective velocities everywhere and large scale convective motions are hindered.

One of the most interesting observation here concerns the segregation dynamic at intermediate regime ($5 \times 10^{-3} < \epsilon < 0.05$). In Figure 4, for $\epsilon = 5 \times 10^{-3}$ and $\epsilon = 0.01$, segregation is ongoing. Some crystals have already accumulated at the bottom and melt has been extracted at the top (see Figure 4c). We observe in Figure 4a, that the separation velocity dominates the dynamics in the center of the convective cells and below the

Figure 3. Statistical distribution of vertical convective velocities (v_z , red histograms) and vertical settling velocities (Δv_z , blue histograms) at $t^* = 0$ (a) and $t^* = 0.0005$ (b) ($Ra = 10^6$, $\zeta = 1$, $B = 2$, no phase change). We have investigated five values of mixture size: 0.5×10^{-3} , 1×10^{-3} , 5×10^{-3} , 0.01 and 0.05. The vertical heights of the histograms are proportional to the volume of the flow having a given velocity. The red line represents the average velocity at $Ra=10^6$ predicted by a scaling law [Pandey *et al.*, 2014]. The blue line represents the solution at infinity of the phase separation velocity, see (30). Two snapshots of the flows in the cases with $\epsilon = 5 \times 10^{-3}$ and $\epsilon = 0.01$ are depicted in Figure 4.

top boundary layer and above the bottom boundary layer, for $\epsilon = 0.01$. This observation corroborates previous findings that have shown that crystal settling should be particularly efficient at the top and bottom boundary of the convective region where vertical convective velocities cancels [Tonks and Melosh, 1990; Spera, 1992]. However, even if this simple analysis remains acceptable in 1D in the vertical direction, caution must be applied in 2D. We see in Figure 4b that regions where phase separation is efficient (in red in Figure 4a) are not necessarily associated with regions where crystals accumulate (in red in Figure 4b). Lateral motion is able to sweep crystals in these boundary layers [Tonks and Melosh,

Figure 4. 2D fields of (a) the difference between $|\Delta v_z|$ and $|\bar{v}_z|$ ($Ra = 10^6$, $\zeta = 1$, $B = 2$, no phase change) (b) accumulation rate, i.e., $\partial_t \phi$, (c) melt fraction and (d) temperature. These picture are snapshots of the two simulations ($\epsilon = 5 \times 10^{-3}$ and $\epsilon = 0.01$) discussed in Figures 2 and 3. Regions where phase separation is efficient (in red in panel a) must not be associated with regions where crystals accumulate (in red in panel b).

1990; Solomatov and Stevenson, 1993a]. In Figure 4b, regions of high accumulation rate in the bulk correspond to the re-entrainment of crystals by the convective flow at the top of transient dunes. In the top and bottom regions where vertical convective motions are very small, the stronger the phase separation (i.e., the larger the mixture size), the more difficult the crystal sweeping is. The height of the dunes is therefore larger for $\epsilon = 5 \times 10^{-3}$ than for $\epsilon = 0.01$.

We have shown that our approach is able to model crystal settling in a consistent way. The threshold at which the regime change from crystal re-entrainment to settling has been identified ($\epsilon \sim 5 \times 10^{-3}$ for $Ra = 10^6$, $B = 2$). Consequently, we are able to set our dynamic model either in non-fractional crystallization or fractional crystallization mode by varying the mixture size. Notice however, that porosity and crystal size are implicitly related in our model while they should be independent variables. This obviously limits our ability to account accurately of the local scale aspects of crystal settling such as clustering. Our separation velocity as a function of phase content (see 30) is symmetrical with respect to $\phi = 1/2$ while a more sophisticated parametrization could be implemented. The physics of crystal growth is also not considered explicitly in our model, but only indirectly through the changes in the average liquid fraction. The major advantage of our mathematical framework compared to other work is to couple easily settling with phase change. We describe in the next section some effects of phase change in such multiphase system where solids can crystallize float, settle or remelt.

4 Phase change and density contrast

In a crystallizing and convecting system, the location of the adiabat compared to the liquidus and the solidus defines at first order the thermodynamic stability of crystals (more complexity might be required if we consider that melting temperature depends on chemical composition). For small planetary bodies such as the Moon or Vesta, it is generally accepted that the adiabat lies in between liquidus and solidus during crystallization [Elkins-Tanton, 2012]. In this case, it turns out that we may neglect crystal dissolution during magma ocean crystallization. In the case of magma ocean in larger planetary bodies, the isentropic temperature may be higher than the liquidus either at shallow depth (if magma ocean crystallizes from the bottom to the top) or at the bottom of the mantle (top down crystallization, e.g., [Stixrude *et al.*, 2009]) or both. In the case of the Earth, it thus becomes important to couple melting/dissolution with crystal settling as both density contrast and density cross-over between melt and crystals might lead to more complex style of crystallization [Labrosse *et al.*, 2007].

For the sake of simplicity, we consider here the mantle as a univariant system. In a simple univariant phase transition there is a relation (the Clapeyron relation) between the latent heat L , the density difference between phases ρ_1 and the slope of the melting curve dT/dz . However what we try to model is far from a simple univariant transition. First,

the slope of the melting curve that we introduce stands in fact for the difference between a real melting curve and an adiabatic gradient which is not accounted for by the incompressible equations. Second the liquid and solid phases in mantle silicates should not have the same composition; typically the liquid should be iron and aluminium rich, and might be lighter or denser than the magnesium rich solid at equilibrium [Boukaré *et al.*, 2015]. Therefore we consider the melting curve, the Stefan number and the buoyancy number B as independent quantities.

We use a temperature of melting which increases linearly with depth so that solids are formed in the deepest half where they can be negatively, neutrally or positively buoyant. For the sake of simplicity, the melting curve has been chosen linear and in such a way that the stationary solutions do not show phase changes near the boundary layers (i.e. the melting temperature is -0.1 on top, 1.1 at the bottom). The slope of the melting curve is thus particularly large to insure that melt is stable at the surface and solid at the bottom. In the following simulations, there is no viscosity variation in the average viscosity although the low viscosity melt can separate from the matrix as implied by the separation velocity (7).

4.1 Bottom-up crystallization dynamics with negatively or neutrally buoyant crystals

We start with simple scenarios to test the effects of the Stefan number and of a positive buoyancy number B . The mixture characteristic size is set to $\epsilon = 0.1$ so that phase separation occurs easily. We show in Figure 5 three depth-dependent profiles of simulations with different buoyancy and Stefan numbers. To characterize the dynamics, we plot the horizontal averaged temperature (red), melt fraction (blue) and melting curve (green) (Figure 5, left column) and the contributions responsible for the heat transfers (see 26): advection (red), diffusion (green) and latent heat release (blue) (Figure 5, right column). At steady state or when averaged in time, the sum of the three energy transfers (magenta) should remain constant with depth. Figure 5a depicts the reference case where the Stefan number, St , and the buoyancy number, B , have been set to 0.3 and 0 (i.e. no density difference), respectively. In Figure 5b, we double the Stefan number from 0.3 to 0.6. In Figure 5c, we increase the buoyancy number from 0 to 0.5 for a Stefan number of 0.3 like in panel (a).

First, we observe that the 1D temperature profiles in the shallow and deep magma oceans are very similar to what is expected from incompressible thermal convection: energy transfer by advection (red) is replaced by diffusion (green) in the top and bottom boundary layers (Figure 5, right column). In the mushy zone, advection is replaced by both latent heat exchange (blue) and diffusion (as a temperature gradient is imposed by the melting curve). Latent heat release during melting generates a temperature jump which is located here in the middle of the box due to the choice of the melting curve. As expected, the temperature jump is close to the Stefan number, about 0.6 in Figure 5b which does not reach a steady state pattern, whereas it is about 0.3 in Figure 5a. For $B = 0$, the depth over which the temperature jump occurs is controlled by the Stefan number and the slope of the melting curve.

In the case of neutral buoyancy between melt and solid ($B = 0$, Figure 5 panels a and b), the 1D averaged melt fraction goes linearly from 0 to 1 in the mushy zone as temperature variation is proportional to melt fraction variation during phase change. In the case of buoyant melt ($B = 0.5$), liquids are extracted from the slurry layer to the top. We can clearly observe that the mushy zone is very thin in this situation (Figure 5c). Corresponding snapshots of the composition and temperature are depicted in Figure 6. Solids are formed in the cold downwellings plumes; due to their high density, they sink, accumulate and compact at the top of the solid layer. We can also observe partial melting occurring in hot upwelling plumes (Figure 6). The dynamics of the shallow layer is dominated by cold instabilities sinking in a passive medium, while on the contrary, rising hot plumes are only active in the bottom crystallized layer. The temperature of the hot plumes in the shallow layer is comparable to that of the cold plumes in the deep layer.

4.2 Bottom-up crystallization dynamics with buoyant crystals

We test the effects of buoyant crystals ($Ra = 10^6$, $\zeta = 1$, $B = -0.5$) for three different mixture characteristic sizes: $\epsilon = 0.1$, $\epsilon = 0.05$ and $\epsilon = 0.01$. The melting curve remains the same as that used for the previous simulations. The solids are still formed in the deepest half but are now lighter than the liquid (see Figure 7 showing the met fraction

Figure 5. Horizontal averaged profiles of temperature and melt fraction (left) and energy transfer (right), ($Ra = 1 \times 10^6$, $\zeta = 1$, $\epsilon = 0.1$). Partial and total heat fluxes have been normalized by the common maximum of the three partial fluxes (advection, diffusion and latent heat transport). (a) $S_t = 0.3$ et $B = 0$. The mid mantle temperature jump is governed by the latent heat release (the Stefan number). Without density contrast between melt and solid, the thickness of the mushy layer is controlled by the slope of the melting curve and the latent heat. In the mushy zone, energy transfer by advection is replaced by both diffusion (induced by the slope of the melting curve) and latent heat exchanges. The system reaches here a stationary state (i.e. the sum of the heat fluxes remains constant at all depth). (b) $S_t = 0.6$ and $B = 0$. For a given melting curve slope, the larger the Stefan number, the larger the thickness of the mushy layer is. Note that we do not get a stationary state in this case. (c) $S_t = 0.3$ and $B = 0.5$. As the slope of the melting curve is positive and melt is buoyant, melt extraction towards the top reduces the thickness of the mushy zone.

and the temperature for simulations done with different ϵ). When solids are buoyant, they rise and remelt after being formed at the bottom of the domain (due to the location of the melting curve in our simulations). Solids snow across the magma ocean from the bottom to the top (although in this simulation the snow moves upward and is depicted in black in the figures). The snow regime exhibits a chimney-like pattern. The energy carried by latent heat is transported from the top to the bottom of the domain. Consequently, the total output heat flux is decreased compared to the previous simulations as the contribution of the latent heat release to the flux is negative. The freezing and remelting of the solids bring the temperature close to the melting temperature profile almost everywhere. Due to

Figure 6. Snapshots of compositional and temperature fields of a crystallizing system ($Ra = 10^6$, $\zeta = 1$, $B = 0.5$, $\epsilon = 0.1$). Solids are denser than liquids. Solids are formed in the cold downwellings plumes. Due to their high density, they sink, accumulate and compact at the top of the solid layer. The mushy layer is thus very thin. In the bottom layer, partial melting is observed in the head of hot plumes. Associated heat flux and horizontal averaged quantities are presented in Figure 5c.

the fact that the melting curve is slightly below 0 on top and above 1 at the bottom, the temperature can be locally negative or larger than 1 (in green).

If phase separation is easy (large ϵ), crystals can accumulate at the top of the domain before remelting ($\epsilon = 0.1$, Figure 7a). Although the temperature is close to the melting temperature, some large-scale thermal convection still occurs. For intermediate mixture characteristic sizes ($\epsilon = 0.05$, Figure 7b), crystals cannot accumulate. An interesting feature is that pure thermal convection seems to shut down (whereas it remains active for $\epsilon = 0.1$) ; all the heat flow is now transported by latent heat and conduction. For small mixture size ($\epsilon = 0.01$, Figure 7c), the crystals rise so slowly that they accumulate where they are formed, then remelt totally before reaching the top of the domain. The temper-

ature at the top and bottom boundary layers is therefore not buffered by the liquidus and we do not observe out of scale temperature near the boundary layers in Figure 7c. Right on top of the region where crystals are formed, the crystal fraction is higher than in the case of larger ϵ . The size of the mushy region is here governed by the Stefan number, the slope of the melting curve, the mixture characteristic size and the buoyancy number. The fact that we do not observe the chimney-like snow pattern for $\epsilon = 0.01$ might be due to a too coarse grid resolution. Later in the simulation corresponding to Figure 7c, a large-scale Rayleigh-Taylor instability develops as the solid bottom layer is gravitationally unstable and this largely remelts the solid. This evolution of a growing deep solid layer punctuated by Rayleigh-Taylor instabilities is somewhat forced by the fixed bottom temperature condition and should rather be studied in a real cooling situation (e.g. imposing a zero or a decreasing in time bottom heat flux).

Figure 7. Snapshots of compositional and temperature fields of a system crystallizing from the bottom with buoyant crystals ($Ra = 10^6$, $\zeta = 1$, $B = -0.5$). As the temperature tends to follow the melting curve (linear between -0.1 on top and 1.1 at the bottom, like in Figure 5), the temperature can locally be slightly negative or slightly larger than 1 (in green). As soon as crystals are formed at the bottom of the domain, they rise. Solids snow upward across the magma ocean from the bottom to the top (with our color scale the rising snow is depicted in black). Snow pattern depends on the mixture characteristic length. (a) $\epsilon = 0.1$. The phase separation speed is so large that crystals can accumulate at the top of the domain before remelting. (b) $\epsilon = 0.05$. Rising time is comparable to melting time. (c) $\epsilon = 0.01$. Crystals accumulate at the bottom but remelt completely before having reached the top of the domain as phase separation speed is too slow.

5 Application to the Earth's magma ocean

5.1 Solids denser than the fluid

During the past three decades, experimental constraints on melting temperature of silicate material (e.g., *Ohtani* [1983], *Takahashi* [1986], *Zhang and Herzberg* [1994], *Andrauli et al.* [2011]) have proposed that mantle liquidus remains super-isentropic [*Thomas et al.*, 2012; *Mosenfelder et al.*, 2009] in the deep mantle and should cross the magma ocean geotherm (i.e., isentrope) at the bottom of the mantle. This thermodynamic data thus favor scenarios where mantle crystallizes from the bottom up [*Solomatov*, 2000]. In this case, it has been shown that mantle crystallization is a fast process that can reach solid-state behaviour in 20 kyrs and be totally achieved in a few hundred million years (e.g., *Abe* [1993], *Elkins-Tanton* [2008], *Monteux et al.* [2016]). Assuming that liquids remain buoyant at all mantle depth, the issue of primitive mantle differentiation remains either on the efficiency of crystals settling in highly turbulent magma ocean or subsequent melt percolation once melt fraction has crossed the rheological transition (e.g., *Solomatov and Stevenson* [1993b], *Solomatov and Stevenson* [1993c], *Solomatov and Stevenson* [1993a]).

However, if mantle crystallization does not occur from the bottom up, the evolution must be revisited. *Labrosse et al.* [2007] have proposed that crystallization might have started at mid-mantle. Indeed, liquidus and geotherm might intersect at first within the lower mantle (e.g., *Fiquet et al.* [2010]). In such case, the upper magma ocean crystallizes in the same way as described above (i.e., rapidly) but the crystallization of the deep mantle is very slow as heat is extracted by solid-state convection occurring in the overlying young solid mantle. However in the scenario proposed by *Labrosse et al.* [2007], it is not clear why the first solids that appear in the mid-mantle should stay there unless they are in gravitational equilibrium with the surrounding liquid. Dense solids formed on top of the deep magma ocean might sink (snow) toward the core and remelt in a situation reverse to what was described in Figure 7a (in Figure 7a a light solid crystallizes at depth and rises, while in a deep magma ocean, solids may form on top and sink). This melting should cool the deepest layers, bring them to the liquidus and then the crystallization of the deep mantle might occur from the bottom up. The deep magma ocean scenario of *Labrosse et al.* [2007] and *Labrosse* [2016] seems to require that liquids become denser than solids at some depth.

5.2 A solid-liquid density cross-over

We now investigate the dynamic of a crystallizing system when the crossing between liquidus and isentrope does not coincide with the density cross-over between melt and solid. We address this problem in the case where liquidus first intersects the geotherm at the bottom of the mantle with a density cross-over at mid-mantle depth.

The numerical simulation is set up as follows. Even though our multiphase model only handles one-component composition, we want to anticipate the fact that liquids might become denser than solids at deep mantle conditions due to iron enrichment of the liquid phase (e.g., *Boukaré et al.* [2015]; *Nomura et al.* [2011]). We define a depth-dependent buoyancy number which generates buoyant melt only in the upper part of the mantle. For the sake of simplicity, the buoyancy number is linear with depth and the depth of the density inversion is located in the middle of the mantle,

$$B = 2z - 1 \quad (33)$$

Even though the location of the density inversion between melt and solid is intimately linked to the intersection between liquidus and isentrope (via thermodynamic rules), we choose here to consider them as independent parameters. The liquidus temperature is linear (which breaks thermodynamic self-consistency for monovariant systems as we set depth-dependent density contrast between melt and solids). To be consistent with an incompressible flow, its slope is determined by subtracting the experimental super-isentropic liquidus of *Andrault et al.* [2011] ($\approx 0.83 \text{ K km}^{-1}$) to the isentropic profile of *Thomas et al.* [2012] ($\approx 0.6 \text{ K km}^{-1}$) which gives the following dimensionless liquidus curve, (assuming $\Delta T/H \approx 1 \text{ K km}^{-1}$)

$$\left(\frac{\partial T}{\partial z}\right) = 0.23 \quad (34)$$

The Rayleigh number is only moderately increased, $Ra = 10^7$, in order to preserve the validity of our numerical scheme. Top ($T = 0$) and bottom ($T = 1$) temperatures are imposed. We start with a fully molten system where the temperature is set to 1 everywhere and the mixture characteristic lengths is $\epsilon = 0.1$.

Figure 8 depicts the temperature and melt fraction 2D fields at four timesteps. Horizontally averaged heat fluxes (normalized for each snapshot by the maximum value) are shown on the right panels. At the onset of the mantle crystallization (Figure 8a), the temperature is too high to maintain a significant amount of crystals below the liquidus temper-

ature. Crystals are formed in the cold downwellings but remelt rapidly. Although the 1D averaged profiles intersects the liquidus at the bottom of the mantle, crystals appear in the upper half of the mantle. The temperature decreases progressively in the deep mantle due to the descent of cold material sinking from the top. In the deep mantle, buoyant crystals snow (upward) and remelt during their ascent (Figure 8b). Remelting of ascending silicate material has a negative contribution on the heat flux (see the flux of latent heat in Figure 8). The mean temperature of the mushy region follows the liquidus as the latent release during remelting of the very first solids buffers the temperature. The melt fraction remains relatively high. Notice that the 2D pattern of temperature and composition is far from what could have been guessed from the 1D profiles. Crystals start to accumulate when the snow front reaches the depth of the density inversion (Figure 8c). This is possible because the temperature at the depth of the density cross-over is now below the liquidus temperature. Both the snow from the deep mantle and the cold plumes sinking from the surface feed the neutral buoyancy zone in crystals. When crystal fraction reaches the rheological transition in the neutral buoyancy zone, the upper and lower mantle are mostly decoupled by a solid layer (Figure 8d). From that point on, the high viscosity contrast between the solid shell and the magma oceans (not modeled here) should drastically decrease the heat extraction of the new-formed basal magma ocean. The crystallization of the upper mantle should proceed in the canonical style (from the deep solid shell upward) as crystals are denser than liquid in this shallow region. Notice however, that our model fails at generating two independent magma oceans: the top and bottom magma ocean remain connected through hot plumes in Figure 8c in a way quite similar to mechanism proposed in *Ricard et al.* [2014] where plumes could cross through the lithosphere of young planets.

A movie of the complete simulation ($Ra = 10^7$, $\zeta = 1$, $\epsilon = 0.1$ and $B = 2z - 1$) is available online in the Supplementary Material. It covers a normalized time of 0.02. The bottom temperature being fixed (no core secular cooling), the bottom magma ocean cannot entirely crystallize.

5.3 Discussion

This simulation should definitely not be regarded as a realistic prediction for the crystallization of the Earth's mantle but rather as an attempt (albeit oversimplified) to

Figure 8. Evolution of a crystallizing mantle. The slope of the liquidus is consistent with a super-adiabatic liquidus which intersects the geotherm at the bottom of the mantle. We set the buoyancy number in such way that liquids are buoyant only in the top half of the mantle ($B = 2z - 1$, $Ra = 10^7$, $St = 0.3$, $\zeta = 1$). (a) Onset of crystallization. The first solids appear in cold downwelling plumes. They move towards the surface and remelt. (b) Solids snow across the crystallizing magma ocean. The temperature of the mushy region is decreased to the liquidus by the latent release during remelting of the rising crystals. (c) Formation of stable (chemically and gravitationally) solids. The snow front reaches the neutral buoyancy zone which allows crystals to accumulate. The mean melt fraction remains very high in the deep mantle. (d) Formation of a long-lived solid layer. The melt fraction has crossed the limit that defines the rheological transition from liquid to solid behavior. The evolution of the upper magma ocean and the basal magma ocean are now decoupled.

propose a dynamic model for the generation of a basal magma ocean. Beyond the fact that we cannot model magma ocean dynamics in a realistic regime due to numerical constraints, many aspects of this simulation remain unrealistic. The isoviscous approach for the average flow or the crude law for phase separation, adopted here for the sake of simplicity, overlook major aspects of the dynamics of a solid-liquid system. There is an abundant room for further progress related to these aspects.

The mixture characteristic length (a proxy for solid particle radiuses) has been set arbitrarily to a relatively high value ($\epsilon = 0.1$) in Figure 8. We verified that reducing ϵ down to 5×10^{-3} while keeping $Ra = 10^7$, does not change qualitatively the scenario with a solid layer formed near the solid-liquid density cross-over, not where the first solids crystallize. The present study thus suggests that a mid-mantle density cross-over is able

to generate a basal magma ocean even though the location of the liquidus/geotherm intersection is at the bottom of the mantle. The latter controls the appearance of the very first crystals (i.e., thermodynamic equilibrium). The density contrast brings crystals towards the region of neutral buoyancy which perturbs the geotherm in such a way that this region of gravitational equilibrium tends to become the region of solid-liquid thermodynamic equilibrium.

For a given Rayleigh number, it is likely that if ϵ is decreased further, the system might never reach a gravitational equilibrium (the case $Ra = 10^7$ and $\epsilon = 5 \times 10^{-3}$ should correspond to the advection of particles of radius $R = 15.9$ km). The new crystals may simply pile up where they formed, at the bottom of the mantle. The dynamics would therefore be similar to what was illustrated in Figure 7. For a fast phase separation (Figure 7a), the solid phase concentrates where it is gravitationally stable, not where it forms, for a slow phase separation (Figure 7c), the solid phase agglomerates where it forms. However a deep solid layer would be gravitationally unstable and may later undergo a Rayleigh Taylor instability that will bring the dense liquid phase near the core.

The crudest assumption here remains the parametrization of the chemistry effects on the buoyancy number. According to the current constraints on density contrast between melt and solid at deep mantle conditions, two end-members cases can be considered if we follow the idea that iron-rich and aluminium-rich silicate liquids became denser than magnesium-rich solids at the CMB. Either the first crystals formed at thermodynamic equilibrium with an undifferentiated melt at the bottom of the magma ocean were already buoyant at the onset of the crystallization, *or* they became progressively buoyant because of the melt progressive enrichment in iron due to fractional crystallization.

We have somehow modeled here the former case and we can only speculate to what would happen in the second case. In the case of chemical fractionation, a numerical code would need at least four chemical species (two chemical end-members, a heavy and a light component, in each mechanical phase) to mimic the chemical evolution of the system [see e.g., *Wallner and Schmeling*, 2016]. The point is that the compositions of the two mechanical phases (solid and liquid) would not be homogenous and the model would need to accurately simulate the mixing (by advection or diffusion) of the end-members inside the two phases to estimate consistently the density contrast between melt and solid. This might be one of the most important issue for future research on the dynamic of multi-

component crystallizing systems. The locations of the region where thermodynamic equilibrium between crystals and liquid is possible, and the region where both solids and liquids have the same intrinsic density would change through time. Here again, if phase separation is fast enough, crystallization would occur near the region of density cross-over, if phase separation is too slow, gravitationally unstable layers may form, punctuated by Rayleigh-Taylor instabilities.

Notice, that we have not considered the mantle secular cooling as we have imposed fixed temperatures at the top and bottom boundaries. Taking into account the secular cooling would impose to also simulate or parametrize the behavior of the core and its coupling with the mantle. The main complexity of magma ocean dynamics relies on the feedbacks between various timescales (secular cooling, convective and separation time scales) and the spatial distribution of solids.

6 Conclusions

By using a two phase formalism, we are able to simulate the crystallization of a liquid in conditions that can illustrate various situations that took place during the solidification of the mantle. Although the parameter space that we can explore is far from being realistic, we capture various phenomenon such as stable solidification (simultaneous thermodynamic and gravitational stability) or unstable solidification (thermodynamic stability with gravitational instability). This latter instability can be associated with the formation of a homogeneous snow regime, of chimneys or of Rayleigh Taylor instabilities depending of the ease of phase separations. These different types of stable or unstable crystallization could have existed simultaneously at different depths of the Earth.

The fractionation of heavy elements between the solid and liquid phases has been suggested to be associated with a cross-over between the solid and the liquid phases. A simple simulation of the situation where this density cross-over is only depth-dependent and phase separation is easy, suggests that the solid phase likely accumulates where the density cross-over occurs, rather than where the solids initially form. This is because a transient snow regime brings the geotherm to a situation where the depth of gravitational stability becomes also that of thermodynamic stability. The situation where the density cross-over would also be time-dependent due to the progressive enrichment of the melt in

heavy elements has not been considered here as it would need to account locally for the phase change of at least a bivariant equilibrium (two solid and two liquid phases).

Acknowledgments

We thank Harro Schmeling and an anonymous reviewer for their thorough comments on the first version of this paper. This research was funded by ANR-2010-BLAN-622-01 "CMB Melt". Data can be found in the figures and the physical parameters used to produce the figures are listed in Table 1 and 2.

References

- Abe, Y. (1993), The evolving Earth physical state of the very early Earth, *Lithos*, 30(3), 223 – 235, doi:[http://dx.doi.org/10.1016/0024-4937\(93\)90037-D](http://dx.doi.org/10.1016/0024-4937(93)90037-D).
- Andrault, D., N. Bolfan-Casanova, G. L. Nigro, M. A. Bouhifd, G. Garbarino, and M. Mezouar (2011), Solidus and liquidus profiles of chondritic mantle: Implication for melting of the Earth across its history, *Earth Planet. Sci. Lett*, 304, 251 – 259, doi:<http://dx.doi.org/10.1016/j.epsl.2011.02.006>.
- Andrault, D., S. Petitgirard, G. L. Nigro, J.-L. Devidal, G. Veronesi, G. Garbarino, and M. Mezouar (2012), Solid-liquid iron partitioning in Earth's deep mantle, *Nature*, 497(7407), 354–357, doi:10.1038/nature11294.
- Batchelor, G. K. (1967), *An introduction to fluid dynamics*, Cambridge University press.
- Bercovici, D., and Y. Ricard (2003), Energetics of a two-phase model of lithospheric damage, shear localization and plate-boundary formation, *Geophys. J. Int.*, 152(3), 581–596.
- Bercovici, D., Y. Ricard, and G. Schubert (2001), A two-phase model for compaction and damage: 1. General theory, *J. Geophys. Res.: Solid Earth*, 106(B5), 8887–8906, doi:10.1029/2000JB900430.
- Boukaré, C.-E., Y. Ricard, and G. Fiquet (2015), Thermodynamics of the MgO-FeO-SiO₂ system up to 140 GPa: Application to the crystallization of Earth's magma ocean, *J. Geophys. Res.: Solid Earth*, 120(9), 6085–6101, doi:10.1002/2015JB011929.
- Canup, R. M. (2008), Accretion of the earth, *Philosophical Transactions of the Royal Society A: Mathematical, Physical and Engineering Sciences*, 366(1883), 4061–4075.
- Castillo-Rogez, J., T. V. Johnson, M. H. Lee, N. J. Turner, D. L. Matson, and J. Lunine (2009), Al-26 decay: Heat production and a revised age for iapetus, *Icarus*, 204(2), 658–662.

Clift, R., J. R. Grace, and M. E. Weber (1978), *Bubbles, drops, and particles*, Academic Press, 380pp.

Deubelbeiss, Y., B. Kaus, and J. Connolly (2010), Direct numerical simulation of two-phase flow: Effective rheology and flow patterns of particle suspensions, *Earth Planet. Sci. Lett.*, 290(1), 1–12.

Einstein, A. (1911), Berichtigung zu meiner arbeit: "Eine neue bestimmung der moleküldimensionen", *Annalen der Physik*, 339(3), 591–592, doi: 10.1002/andp.19113390313.

Elkins-Tanton, L. (2008), Linked magma ocean solidification and atmospheric growth for Earth and Mars, *Earth Planet. Sci. Lett.*, 271, 181 – 191, doi: <http://dx.doi.org/10.1016/j.epsl.2008.03.062>.

Elkins-Tanton, L. T. (2012), Magma Oceans in the Inner Solar System, in *Annu. Rev. Earth Planet. Sci.*, Vol. 40, edited by Jeanloz, R, pp. 113–139, doi:10.1146/annurev-earth-042711-105503.

Faroughi, S. A., and C. Huber (2015a), A generalized equation for rheology of emulsions and suspensions of deformable particles subjected to simple shear at low reynolds number, *Rheol. Acta*, 54(2), 85–108.

Faroughi, S. A., and C. Huber (2015b), Unifying the relative hindered velocity in suspensions and emulsions of nondeformable particles, *Geophys. Res. Lett.*, 42(1), 53–59.

Fiquet, G., A. L. Auzende, J. Siebert, A. Corgne, H. Bureau, H. Ozawa, and G. Garbarino (2010), Melting of peridotite to 140 gigapascals, *Science*, 329(5998), 1516–1518, doi: 10.1126/science.1192448.

Flasar, F. M., and F. Birch (1973), Energetics of core formation: A correction, *J. Geophys. Res.*, 78(26), 6101–6103, doi:10.1029/JB078i026p06101.

Funamori, N., and T. Sato (2010), Density contrast between silicate melts and crystals in the deep mantle: An integrated view based on static-compression data, *Earth Planet. Sci. Lett.*, 295, 435–440, doi:10.1016/j.epsl.2010.04.021.

Höink, T., J. Schmalzl, and U. Hansen (2005), Formation of compositional structures by sedimentation in vigorous convection, *Phys. Earth Planet. Inter.*, 153, 11 – 20, doi: <http://dx.doi.org/10.1016/j.pepi.2005.03.014>.

Huppert, H. E., and R. S. J. Sparks (1981), The fluid dynamics of a basaltic magma chamber replenished by influx of hot, dense ultrabasic magma, *Contrib. Mineral. Petrol.*, 75(3), 279–289.

King, E., S. Stellmach, and B. Buffett (2013), Scaling behaviour in rayleigh–bénard convection with and without rotation, *J. Fluid Mech.*, 717, 449–471.

Labrosse, S. (2016), Thermal State and Evolution of the Earth Core and Deep Mantle, in *Deep Earth: Physics and Chemistry of the Lower Mantle and Core*, H. Terasaki and R. A. Fischer ed., pp. 43–54, John Wiley & Sons, Inc, doi:10.1002/9781118992487.ch4.

Labrosse, S., J. Hernlund, and N. Coltice (2007), A crystallizing dense magma ocean at the base of the Earth’s mantle, *Nature*, 450, 866–869, doi:10.1038/nature06355.

Maas, C., and U. Hansen (2015), Effects of Earth’s rotation on the early differentiation of a terrestrial magma ocean, *J. Geophys. Res.: Solid Earth*, 120(11), 7508–7525, doi: 10.1002/2015JB012053.

Martin, D., and R. Nokes (1988), Crystal settling in a vigorously converting magma chamber, *Nature*, 332(6164), 534–536.

Martin, D., and R. Nokes (1989), A fluid-dynamical study of crystal settling in convecting magmas, *J. Petrol.*, 30(6), 1471–1500.

McKenzie D. (1984), The generation and compaction of partially molten rock, *J. Petrol.*, Vol 25, 713, doi:10.1093/petrology/25.3.713.

Monteux, J., D. Andraut, and H. Samuel (2016), On the cooling of a deep terrestrial magma ocean, *Earth Planet. Sci. Lett.*, 448, 140 – 149, doi: <http://dx.doi.org/10.1016/j.epsl.2016.05.010>.

Mosenfelder, J. L., P. D. Asimow, D. J. Frost, D. C. Rubie, and T. J. Ahrens (2009), The MgSiO₃ system at high pressure: Thermodynamic properties of perovskite, postperovskite, and melt from global inversion of shock and static compression data, *J. Geophys. Res.*, 114(B1), doi:10.1029/2008JB005900.

Nomura, R., H. Ozawa, S. Tateno, K. Hirose, J. Hernlund, S. Muto, H. Ishii, and N. Hiraoka (2011), Spin crossover and iron-rich silicate melt in the earth’s deep mantle, *Nature*, 473(7346), 199–202.

Ohtani, E. (1983), Melting temperature distribution and fractionation in the lower mantle, *Phys. Earth Planet. Inter.*, 33(1), 12 – 25, doi:[http://dx.doi.org/10.1016/0031-9201\(83\)90003-1](http://dx.doi.org/10.1016/0031-9201(83)90003-1).

Pandey, Ambrish and Verma, Mahendra K and Mishra, Pankaj K (2014), Scaling of heat flux and energy spectrum for very large Prandtl number convection, *Phys. Rev. E*, 89(1), 023006, APS.

Peaceman, D. W., and H. H. Rachford, Jr (1955), The numerical solution of parabolic and elliptic differential equations, *Journal of the Society for Industrial and Applied Mathematics*, 3(1), 28–41.

Pierazzo, E., A. Vickery, and H. Melosh (1997), A reevaluation of impact melt production, *Icarus*, 127(2), 408 – 423, doi:<http://dx.doi.org/10.1006/icar.1997.5713>.

Ricard, Y. (2007), 7.02 - Physics of mantle convection, in *Treatise on Geophysics*, G. Schubert ed., pp. 31 – 87, Elsevier, Amsterdam, doi:<http://dx.doi.org/10.1016/B978-044452748-6.00115-2>.

Ricard, Y., S. Labrosse, and F. Dubuffet (2014), Lifting the cover of the cauldron: Convection in hot planets, *Geochem., Geophys., Geosys.*, 15(12), 4617–4630, doi: 10.1002/2014GC005556.

Roe, P. L. (1985), Some contributions to the modelling of discontinuous flows, in *Lectures in Applied Mathematics*, B. Engquist ed., 22, 163–193.

Sanloup, C., J. W. E. Drewitt, Z. Konôpková, P. Dalladay-Simpson, D. M. Morton, N. Rai, W. van Westrenen, and W. Morgenroth (2013), Structural change in molten basalt at deep mantle conditions, *Nature*, 503, 104–107, doi:10.1038/nature12668.

Schmeling, H., (2000), Partial Melting and melt migration in a convecting mantle in Bagdassarov, N., D. Laporte and A.B. Thompson (eds), *Physics and chemistry of partially molten rocks*, pp. 141-178, Dordrecht: Kluwer Academic Publisher.

Schmeling, H., Kruse, J. , Richard, G., (2012), Effective shear and bulk viscosity of partially molten rock based on elastic moduli theory of a fluid filled poroelastic medium, *Geophys. J. Int.*, Vol 190, 1571–1578, Oxford University Press.

Schubert, G., Turcotte, D. L., Olson, P. (2001), *Mantle convection in the Earth and Planets*. Cambridge University Press.

Solomatov, V. (2007), 9.04 - Magma oceans and primordial mantle differentiation, in *Treatise on Geophysics*, G. Schubert ed., pp. 91 – 119, Elsevier, Amsterdam, doi: <http://dx.doi.org/10.1016/B978-044452748-6.00141-3>.

Solomatov, V. S. (1995), Batch crystallization under continuous cooling: analytical solution for diffusion limited crystal growth, *J. Crystal Growth*, 148(4), 421 – 431, doi: [http://dx.doi.org/10.1016/0022-0248\(94\)00962-7](http://dx.doi.org/10.1016/0022-0248(94)00962-7).

Solomatov, V. S. (2000), Fluid Dynamics of a Terrestrial Magma Ocean, in *Origin of the Earth and Moon*, edited by R. M. Canup, K. Righter, pp. 323–338, The University of Arizona Press.

- Solomatov, V. S., and D. J. Stevenson (1993a), Kinetics of crystal growth in a terrestrial magma ocean, *J. Geophys. Res.: Planets*, 98(E3), 5407–5418, doi:10.1029/92JE02839.
- Solomatov, V. S., and D. J. Stevenson (1993b), Suspension in convective layers and style of differentiation of a terrestrial magma ocean, *J. Geophys. Res.: Planets*, 98(E3), 5375–5390, doi:10.1029/92JE02948.
- Solomatov, V. S., and D. J. Stevenson (1993c), Nonfractional crystallization of a terrestrial magma ocean, *J. Geophys. Res.: Planets*, 98(E3), 5391–5406, doi:10.1029/92JE02579.
- Spera, F. J. (1992), Lunar magma transport phenomena, *Geochim. Cosmochim. Acta*, 56(6), 2253–2265.
- Šrámek, O., Y. Ricard, and D. Bercovici (2007), Simultaneous melting and compaction in deformable two-phase media, *Geophys J. Int.*, 168(3), 964–982, doi:10.1111/j.1365-246X.2006.03269.x.
- Šrámek, O., Ricard, Y., Dubuffet, F., (2010). A multiphase model of core formation. *Geophys. J. Int.*, 181 (1), 198–220.
- Šrámek, O. (2007), Modèle d'écoulement biphasé en sciences de la terre: fusion partielle, compaction et différenciation, Ph.D. thesis, Université de Lyon - Ecole Normale Supérieure, Lyon.
- Šrámek, O., L. Milelli, Y. Ricard, and S. Labrosse (2012), Thermal evolution and differentiation of planetesimals and planetary embryos, *Icarus*, 217(1), 339 – 354, doi: <http://dx.doi.org/10.1016/j.icarus.2011.11.021>.
- Stixrude, L., and B. Karki (2005), Structure and freezing of MgSiO₃ liquid in Earth's lower mantle, *Science*, 310(5746), 297–299.
- Stixrude, L., N. de Koker, N. Sun, M. Mookherjee, and B. B. Karki (2009), Thermodynamics of silicate liquids in the deep Earth, *Earth Planet. Sci. Lett*, 278, 226 – 232, doi: <http://dx.doi.org/10.1016/j.epsl.2008.12.006>.
- Suckale, J., L. T. Elkins-Tanton, and J. A. Sethian (2012), Crystals stirred up: 2. numerical insights into the formation of the earliest crust on the moon, *J Geophys Res.: Planets*, 117(E8), E08,005, doi:10.1029/2012JE004067.
- Takahashi, E. (1986), Melting of a dry peridotite KLB-1 up to 14 GPa - Implications on the origin of peridotitic upper mantle, *J Geophys Res.: Solid Earth and Planets*, 91(B9), 9367–9382, doi:10.1029/JB091iB09p09367.
- Tateno, S., K. Hirose, and Y. Ohishi (2014), Melting experiments on peridotite to lowermost mantle conditions, *J. Geophys. Res.: Solid Earth*, 119(6), 4684–4694, doi:

10.1002/2013JB010616.

Thomas, C. W., Q. Liu, C. B. Agee, P. D. Asimow, and R. A. Lange (2012), Multi-technique equation of state for Fe₂SiO₄ melt and the density of Fe-bearing silicate melts from 0 to 161 GPa, *J. Geophys. Res.*, 117(B10), doi:10.1029/2012JB009403.

Tonks, W., and H. Melosh (1990), The physics of crystal settling and suspension in a turbulent magma ocean., *Origin of the Earth, 1*, 151–174.

Touboul, M., I. S. Puchtel, and R. J. Walker (2012), W-182 evidence for long-term preservation of early mantle differentiation products, *Science*, 335(6072), 1065–1069.

Urey, H. C. (1955), The cosmic abundances of potassium, uranium, and thorium and the heat balances of the earth, the moon, and mars, *Proc. Natl. Acad. Sci.*, 41(3), 127.

Verhoeven, J., and J. Schmalzl (2009), A numerical method for investigating crystal settling in convecting magma chambers, *Geochem. Geophys. Geosyst.*, 10, doi:10.1029/2009GC002509.

Wallner, H. and Schmeling, H., (2016), Numerical models of mantle lithosphere weakening, erosion and delamination induced by melt extraction and emplacement. *Int. J. Earth Sci.*, Vol 105, 1741–1760, doi:10.1007/s00531-016-1343-y.

Yamato, P., R. Tartese, T. Duretz, and D. A. May (2012), Numerical modelling of magma transport in dykes, *Tectonophysics*, 526, 97–109.

Zhang, J., and C. Herzberg (1994), Melting experiments on anhydrous peridotite KLB-1 from 5.0 to 22.5 GPa, *J. Geophys Res.: Solid Earth (1978–2012)*, 99(B9), 17,729–17,742.

Figure 1.

Accepted Article

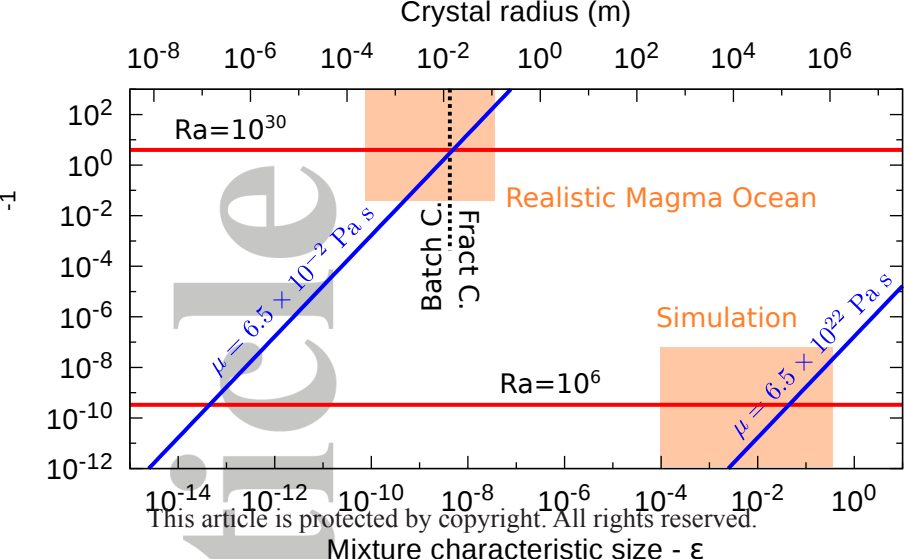


Figure 2.

Accepted Article

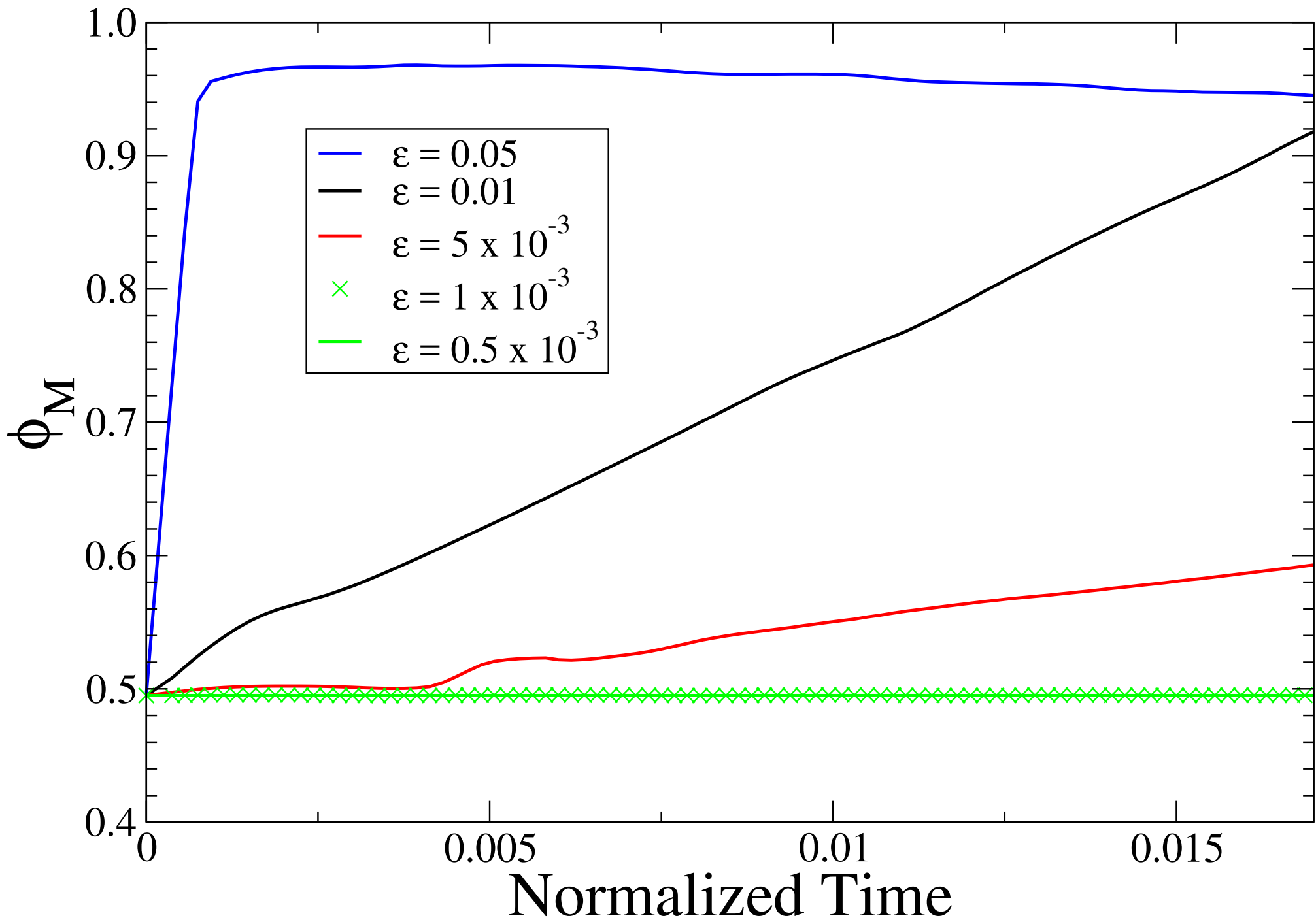
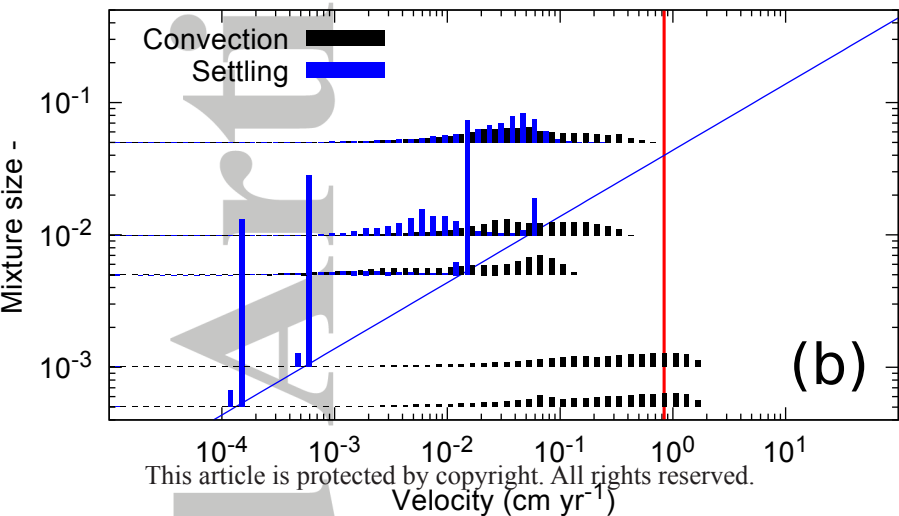
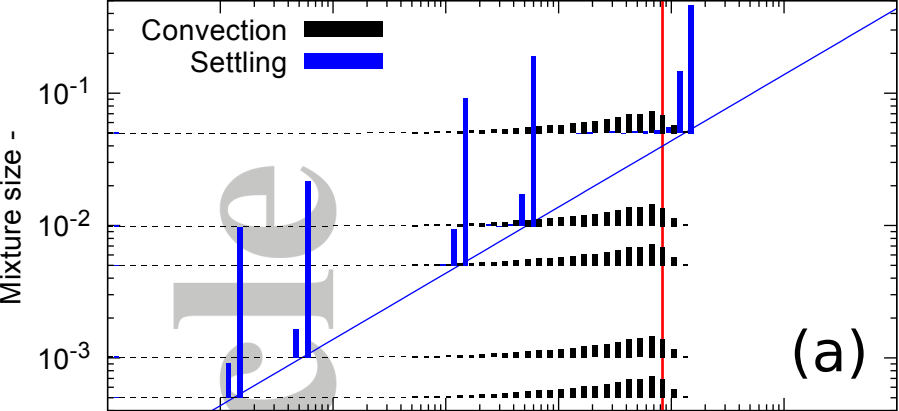


Figure 3.

Accepted Article

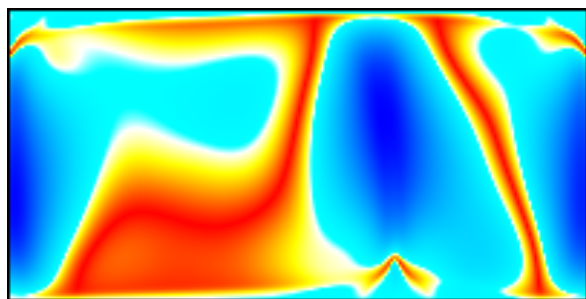
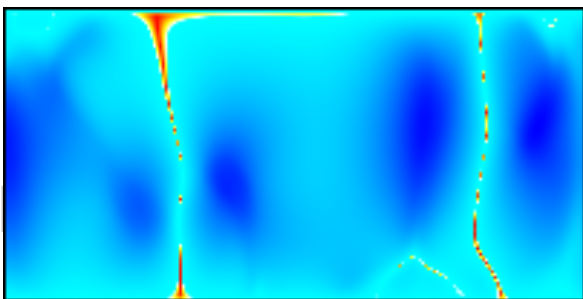
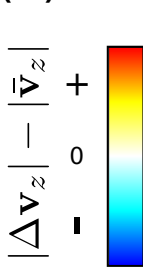


Accepted Article

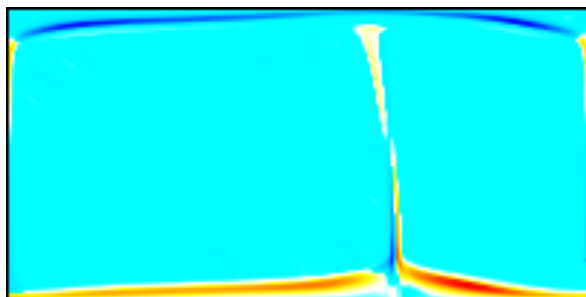
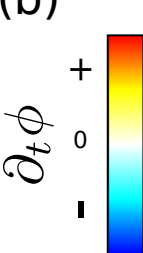
$$\epsilon = 5 \times 10^{-3}$$

$$\epsilon = 0.01$$

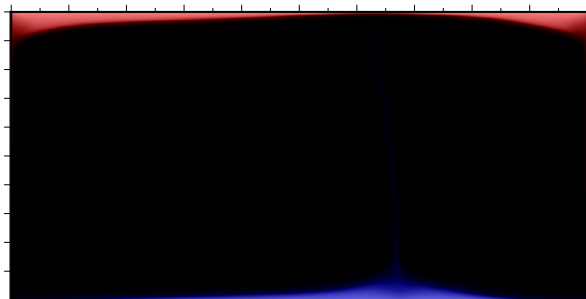
(a)



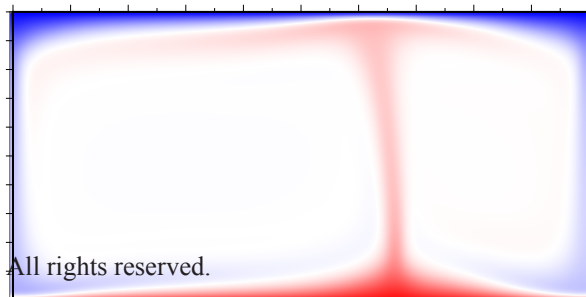
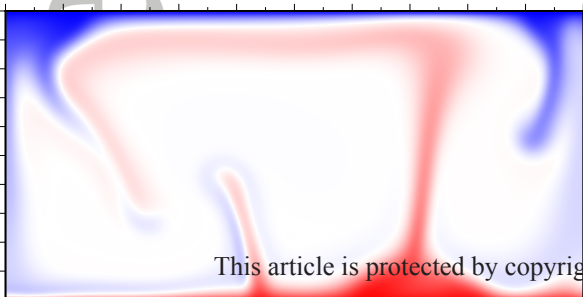
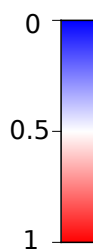
(b)



(c)

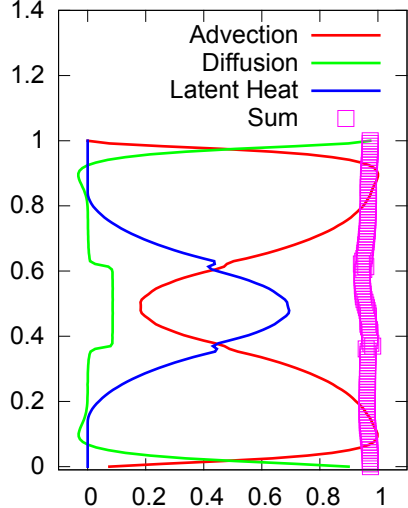
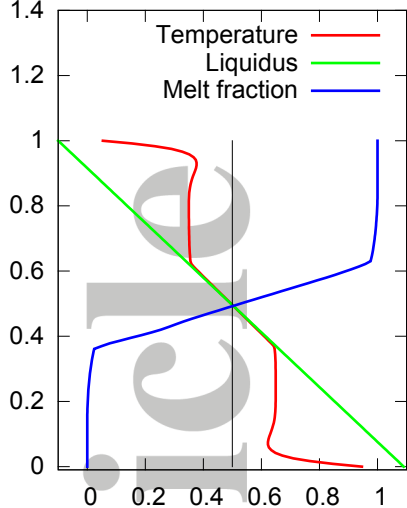


(d)

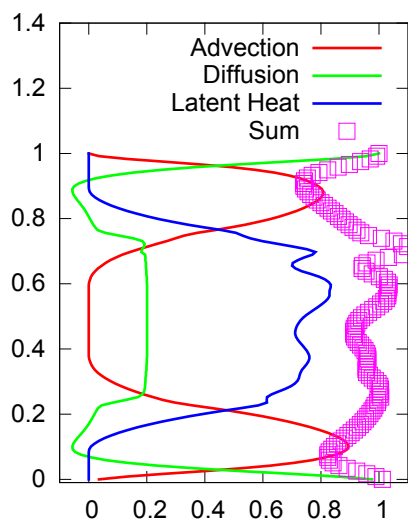
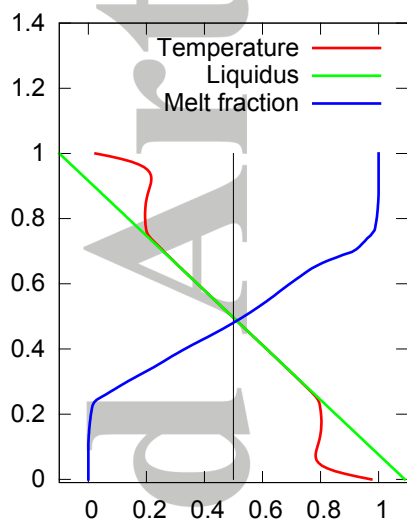


Accepted Article

(a)



(b)



(c)

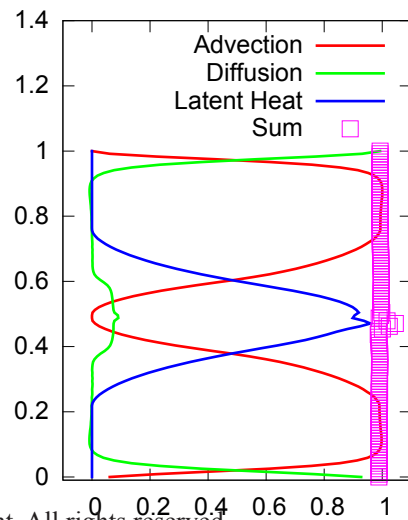
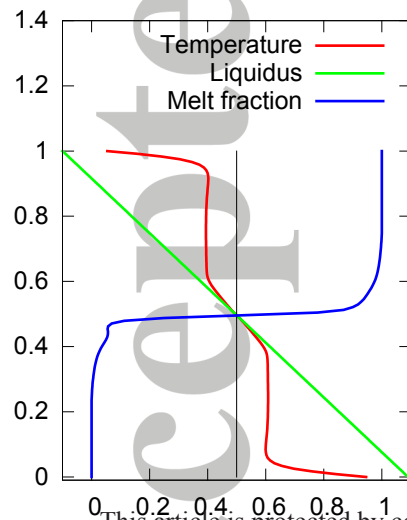


Figure 6.

Accepted Article

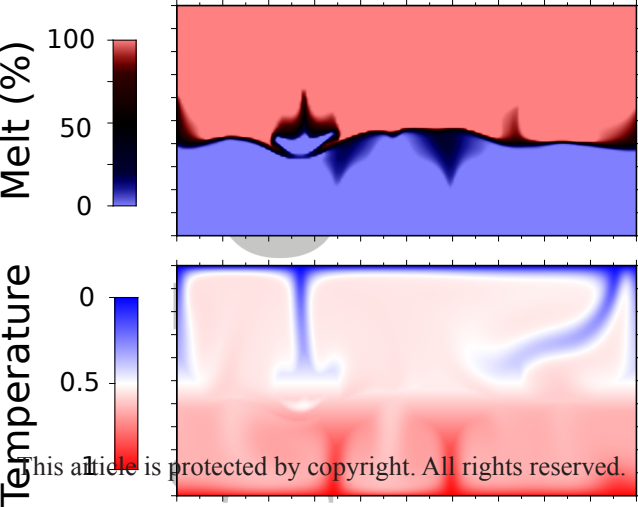
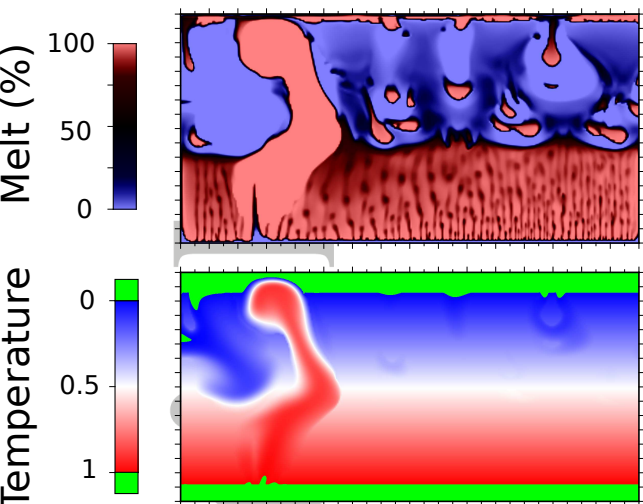


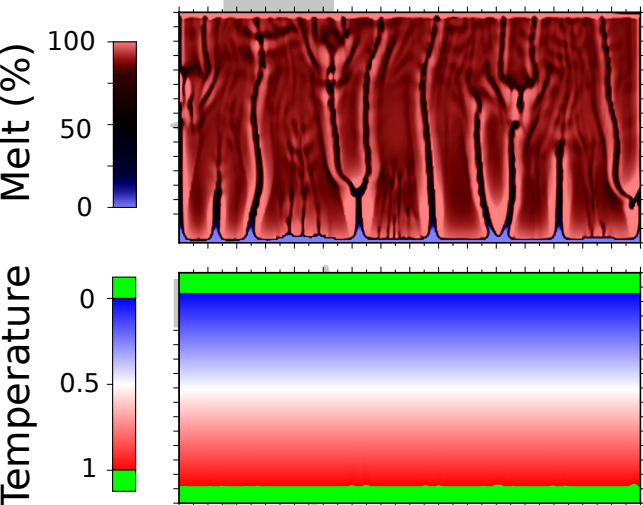
Figure 7.

Accepted Article

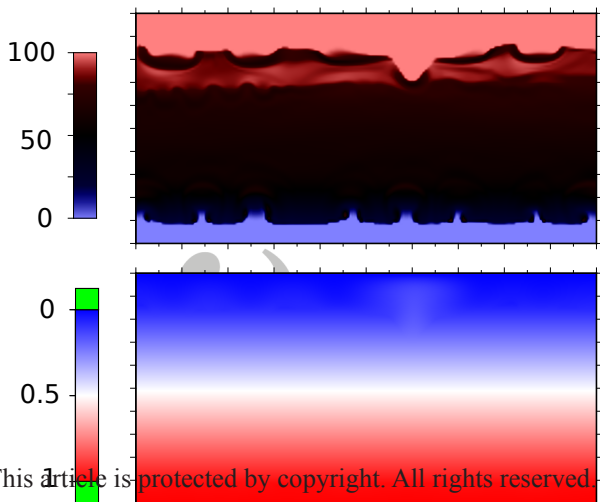
(a) $\epsilon = 0.1$



(b) $\epsilon = 0.05$



(c) $\epsilon = 0.01$



Accepted Article

